Petroleum Science 21 (2024) 2457–2468

Contents lists available at ScienceDirect

Petroleum Science

journal homepage: www.keaipublishing.com/en/journals/petroleum-science

Original Paper

Molecular insights into oil detachment from hydrophobic quartz surfaces in clay-hosted nanopores during steam–surfactant co-injection

Ben-Jie-Ming Liu [a, *], Xuan-Tong Lei [a, **], Mohammadali Ahmadi [a], Zhangxin Chen [a, b, ***]

[a] Department of Chemical and Petroleum Engineering, University of Calgary, 2500 University Dr. NW, Calgary, T2N 1N4, Canada
[b] Eastern Institute of Technology, Ningbo, 315200, Zhejiang, China

ARTICLE INFO

Article history:
Received 27 December 2023
Received in revised form
7 April 2024
Accepted 8 April 2024
Available online 14 April 2024

Edited by Yan-Hua Sun

Keywords:
Clay minerals
Bitumen
Contact angle
Interaction energy
Surfactant
Molecular dynamics

ABSTRACT

Thermal recovery techniques for producing oil sands have substantial environmental impacts. Surfactants can efficiently improve thermal bitumen recovery and reduce the required amount of steam. Such a technique requires solid knowledge about the interaction mechanism between surfactants, bitumen, water, and rock at the nanoscale level. In particular, oil sands ores have extremely complex mineralogy as they contain many clay minerals (montmorillonite, illite, kaolinite). In this study, molecular dynamics simulation is carried out to elucidate the unclear mechanisms of clay minerals contributing to the bitumen recovery under a steam–anionic surfactant co-injection process. We found that the clay content significantly influenced an oil detachment process from hydrophobic quartz surfaces. Results reveal that the presence of montmorillonite, illite, and the siloxane surface of kaolinite in nanopores can enhance the oil detachment process from the hydrophobic surfaces because surfactant molecules have a stronger tendency to interact with bitumen and quartz. Conversely, the gibbsite surfaces of kaolinite curb the oil detachment process. Through interaction energy analysis, the siloxane surfaces of kaolinite result in the most straightforward oil detachment process. In addition, we found that the clay type presented in nanopores affected the wettability of the quartz surfaces. The quartz surfaces associated with the gibbsite surfaces of kaolinite show the strongest hydrophilicity. By comparing previous experimental findings with the results of molecular dynamics (MD) simulations, we observed consistent wetting characteristics. This alignment serves to validate the reliability of the simulation outcomes. The outcome of this paper makes up for the lack of knowledge of a surfactant-assisted bitumen recovery process and provides insights for further in-situ bitumen production engineering designs.

1. Introduction

Despite the significant progress of renewable energy technologies, fossil fuels are estimated to make up half of the global energy consumption by 2050 (Brockway et al., 2019; Welsby et al., 2021). Meanwhile, with the continuous development of the petroleum industry, the pursuit of “easy oil” has become progressively more difficult (Ahmadi and Chen, 2020; Chen et al., 2023). There is an urgent need to exploit unconventional resources to meet the energy demand in the future.

Oil sands, a type of unconventional petroleum deposit, mainly consisting of a mixture of bitumen, quartz sands, clay (e.g., montmorillonite, illite, and kaolinite), and water, have attracted significant research attention at the global scale (Banerjee, 2012; Liu et al., 2019; Lu et al., 2022; Tosuai et al., 2023; Wang et al., 2020). More than 98% of Canada's remaining geological oil reserves are composed of oil sands, making its proven oil reserves the third place in the world (Davenport and Wayth, 2023). However, Canada is suffering from the thermal recovery processes for exploiting these resources, which bring significant challenges such as their complex composition, poor mobility, high operating costs, and

* Corresponding author.
** Corresponding author.
*** Corresponding author. Department of Chemical and Petroleum Engineering, University of Calgary, 2500 University Dr. NW, Calgary, T2N 1N4, Canada.
E-mail addresses: benjieming.liu@ucalgary.ca (B.-J.-M. Liu), xuantong.lei1@ucalgary.ca (X.-T. Lei), zhachen@ucalgary.ca (Z. Chen).

https://doi.org/10.1016/j.petsci.2024.04.004

greenhouse gas emissions (Han et al., 2023; Rui et al., 2018; Tajik et al., 2023; Wang et al., 2022). Recent studies have shown that surfactants can promisingly improve bitumen recovery while simultaneously reducing environmental footprint (Ahmadi and Chen, 2021a; Alshaikh, 2019; Ding et al., 2021; Tackie-Otoo et al., 2020; Tang et al., 2023). However, the impact of surfactants on bitumen recovery has often been assessed too simplistically as improved or deteriorated based on changes in recovery factor. The underlying mechanisms that enhance bitumen recovery under a surfactant-assisted thermal process are not fully understood.

Clay minerals are widely presented in geologic deposits and significantly affect steam-based bitumen extraction recovery and product quality (Czarnecki et al., 2005; Hooshiar et al., 2012; Kaminsky et al., 2009; Sposito et al., 1999). For typical oil sand ores, their solids (mostly sands and clays) can make up ~80% of the total mass (Entezari et al., 2017). It has been found that the distribution of bitumen is influenced by clay concentration, clay structures, and the nanoconfined spaces in porous media (Li et al., 2023; Tian et al., 2019b). The existing literature have different views on clays in crude oil recovery. According to Liu et al. (2004) the presence of clay minerals increases adhesive forces, causing challenges for small bitumen droplets to separate from a rock surface, mainly when calcium ions are present. Xiong and Devegowda (2022) reported that the diffusion of hydrocarbon molecules was impeded in clay-hosed nanopores, resulting from aggregated ions and water bridges, thus reducing the crude oil fluidity. Other studies found that a negative charge on the surfaces of clay minerals makes them a medium for cation exchange, causing adsorption of bitumen and alteration of the rock wettability in nanopores (Cao et al., 2021; Ding and Gao, 2021; Ghaleh et al., 2020; Zhang et al., 2016; Zhong et al., 2013). This shift in rock wettability is favorable for oil-wet and weakly water-wet reservoirs and eventually increases the ultimate oil recovery. Therefore, conducting a comprehensive study to explore the bitumen–solid interactions in clay-hosted nanopores is essential. However, it is labor-intensive and costly for laboratory experimental studies to observe and measure the physicochemical properties of bitumen at the nanoscale.

To date, thanks to the development of computing technologies, molecular dynamics (MD) simulations have been demonstrated to be a powerful tool for gaining fundamental insights into complicated interactions at the molecular level (Koleini et al., 2019; Tian et al., 2019a; Wang et al., 2023). A key strength of MD simulations lies in their ability to reveal the behavior of individual atoms in complex systems where spectroscopic and other conventional experimental methods would probe the average behavior of large numbers of atoms. MD simulations have exhibited great power for investigating interactions between minerals and crude oil. For instance, Zhang et al. (2022) studied the adsorption behavior and interfacial interactions between bitumen and montmorillonite interfaces. They concluded that temperature considerably influences an adsorption configuration and distribution pattern of bitumen on clay surfaces. Yang et al. (2023) found that an increment in the polarity of crude oil components leads to higher binding energy between oil and clays, showing that more heat is generated during adsorption. Underwood and his coworkers used MD simulations to scrutinize the adsorption behavior of crude oil onto basal surfaces of clay minerals (Tian et al., 2018; Underwood et al., 2015). They showed that the adsorption and arrangement of oil molecules depend on the surfaces of clay minerals and the distance away from them. Piri et al. and his coworkers conducted MD simulations to investigate the underlying mechanisms responsible for oil detachment from calcite surfaces under reservoir conditions (Bai et al., 2020; Tetteh et al., 2022; Xie et al., 2020). Additionally, MD simulations can be used to elaborate the complex mechanism of surfactant enhanced oil recovery. Based on MD simulations, Su et al. (2019) found that sodium dodecyl sulfate (SDS) improves the binding ability of bitumen droplets to water molecules, reducing their viscosities under room temperature and pressure. The MD simulation results by Jia et al. (2021) showed that SDS molecules tend to migrate into a heavy oil phase rather than a light oil phase because of the lower Gibbs free energy. Their results proved that a calcite surface became oil-wet due to the adsorption of carboxylate components. Furthermore, they concluded that the oil-wet conditions were more effectively reversed when utilizing a cationic surfactant with an extended molecular length. In a recent study, we conducted a detailed investigation of bitumen detachment from hydrophobic quartz minerals associated with the coexistence of surfactants under realistic thermal recovery conditions (Ahmadi and Chen, 2022). The SDBS molecules had a strong tendency to interact with asphaltene molecules due to $\pi-\pi$ stacking, which is conducive to reduce the oil viscosity.

To the best of authors' knowledge, no work reported using MD simulations to study how the inclusion of clay mineral surfaces affects the interactions between hydrophobic quartz and bitumen droplets. Therefore, the purpose of the present paper is to report the results of such a study in the interlayered systems of oil sands. Four of the most common clay mineral surfaces were studied. We allowed relatively long equilibration times compared to previous MD studies to achieve better observations of in-site interactions between bitumen, water, quartz, and clay minerals. The MD simulation outputs of this study allowed us to gain qualitative and quantitative insights into screening procedures for a thermal recovery process.

2. Models and simulation details

2.1. Models

Unlike organic intercalated clay minerals, the interactions between bitumen and inorganic minerals occurred mainly on the external surface of the minerals. The mineral surfaces of montmorillonite, illite, and kaolinite (siloxane and gibbsite) were selected to study their effects on the oil detachment from hydrophobic quartz surfaces under steam–surfactant co-injection conditions since they are the primary species present in Athabasca oil sands (Carrigy, 1966; Dusseault and Scafe, 1979; Hooshiar et al., 2012). All the minerals used in this study are layered aluminosilicates, where montmorillonite and illite are a 2:1 (two Si–O tetrahedral sheets and an Al–O octahedral sheet) structure, and kaolinite is a 1:1 structure (one Si–O tetrahedral sheet and an Al–O octahedral sheet) (Sposito et al., 1999). Montmorillonite and illite models are generated by the isomorphous substitutions of cations from pyrophyllite, i.e., substitutions of Al^{3+} by Mg^{2+} in the octahedral sheets and of Si^{4+} with Al^{3+} in the tetrahedral sheet (Bickmore et al., 2003; Refson et al., 2003). It is worth mentioning that the isomorphous substitutions in these models obey Loewenstein's rule (Loewenstein, 1954). The Wyoming type of montmorillonite structure is used to describe the molecular structure of Na-montmorillonite, where the simplified formula is $Na_{0.75}(Si_{7.75}Al_{0.25})(Al_{3.5}Mg_{0.5})O_{20}(OH)_4$. That means one Al atom is replaced by an Mg atom in every 8 Al atoms sheet, while one Si atom is replaced by an Al atom in every 32 Si atoms in the tetrahedral in the octahedral sheet. Since the illite extracted from the Athabasca Basin is Mg-poor, we only consider the isomorphous substitutions of Si^{4+} with Al^{3+} (Drits et al., 2010). The resulting chemical formula for the illite model is $K(Si_7Al)Al_4O_{20}(OH)_4$. In contrast to montmorillonite and illite, kaolinite has two different basal surfaces, namely the siloxane and gibbsite surfaces. The unit cell of kaolinite is $Al_4Si_4O_{10}(OH)_4$, where the structural parameters are obtained by X-ray diffraction based on Bish's work (Bish and

Von Dreele, 1989). To simulate the initial wettability of hydrophobic quartz in oil sands, the α-quartz was first cleaved in {1 0 0} direction, and then methyl ($-CH_3$) groups were added to all surface silicon atoms. Such methylated silica surface has been used by many researchers (Deng et al., 2022, 2023; Li et al., 2022). Then, the clay layers were placed parallel to the hydrophobic quartz surface to establish the slit-nanopore model. Herein, the nanopore size of all the slits was kept at a moderate value of 5.0 nm. Fig. 1 shows the process of setting up the nanopore model.

This study employs the classical saturates–aromatic–resin–asphaltene (SARA) model to characterize the bitumen composition. The asphaltene molecule proposed by Badu et al. (2012) is used to build an asphalt model, and the aromatic molecule was based on the study presented by the Verstraete group (Verstraete et al., 2010). Two kinds of resin molecules and saturates are collected from our previous work (Ahmadi and Chen, 2021b). Then, the bitumen droplet was constructed based on a mass fraction of 15:30:35:20, as reported in experimental measurements (Li et al., 2012; Wu et al., 2015). The number of molecules in each fraction is set according to the abovementioned proportion. In addition, sodium dodecylbenzene sulfonate (SDBS) is selected as it exhibits good emulsifying performance under high-temperature conditions (Batmunkh et al., 2016; Kong et al., 2023; Lv et al., 2015). More details of the parameters of simulation systems are provided in Table 1. Table S1 in the Supporting Information provides detailed information on the specific molar fractions of each component and the fundamental physical properties of bitumen. VMD package is employed to visualize all the MD trajectories and configurations in this study. Fig. 2 demonstrates the molecular structure of each fraction.

2.2. Force fields

The extensively implemented CLAYFF force field parameters were adopted to describe the atoms in clay minerals, ions, and hydrophobic quartz due to their accuracy in predicting the properties of bulk nanoporous materials and their interfaces and compatibility with other force fields (Cygan et al., 2004, 2021). It is worth highlighting that the CLAYFF force field does not include parameters for describing atoms in the α-quartz surfaces, namely methyl groups. To this end, the parameters proposed by Deng et al. (2022, 2023) were implemented in the original CLAYFF. The SPC/E model was used to describe the water molecules due to its better performance in calculating water density at high temperatures (Andrés et al., 2015; Berendsen et al., 1987). The SETTLE algorithm was employed to keep water molecules' geometry rigid. The organic molecules in bitumen and surfactant were represented by the OPLS-AA force field (Jorgensen et al., 1996). Their topologies and charges were obtained from the LigParGen server (Dodda et al., 2017). The CLAYFF and the OPLS-AA force fields have been validated in consistent with experimental data and NIST standard database (Zhan et al., 2020; Zhang et al., 2023). The equations of the non-bonded interactions among all atoms were represented by the Lennard–Jones (LJ) 12-6 potential and Coulomb electrostatic interactions, as described in Eq. (1) (Wang et al., 2023):

$$u(r_{ij}) = 4\varepsilon_{ij}\left[\left(\frac{\sigma_{ij}}{r_{ij}}\right)^{12} - \left(\frac{\sigma_{ij}}{r_{ij}}\right)^{6}\right] + \frac{q_i q_j}{4\pi\varepsilon_0 r_{ij}} \quad (1)$$

where r_{ij}, ε_{ij}, and σ_{ij} are the separation distance between atoms, L–J energy, and size parameters, respectively; q_i and q_j are the partial charges of sites i and j; ε_0 is the dielectric constant of vacuum. The Lorentz–Berthelot mixing rules were used to obtain the L–J parameters between different atoms (Eqs. (2) and (3)):

$$\sigma_{ij} = \frac{1}{2}(\sigma_i + \sigma_j) \quad (2)$$

$$\varepsilon_{ij} = \sqrt{\varepsilon_i \varepsilon_j} \quad (3)$$

where σ_i and σ_j are the L–J size parameters of sites i and j; ε_i and ε_j are the L–J energy parameters of sites i and j. The detailed L–J parameters are reported in Table 2.

2.3. Molecular dynamics simulation settings

All MD simulations were carried out using the GROMACS 2021

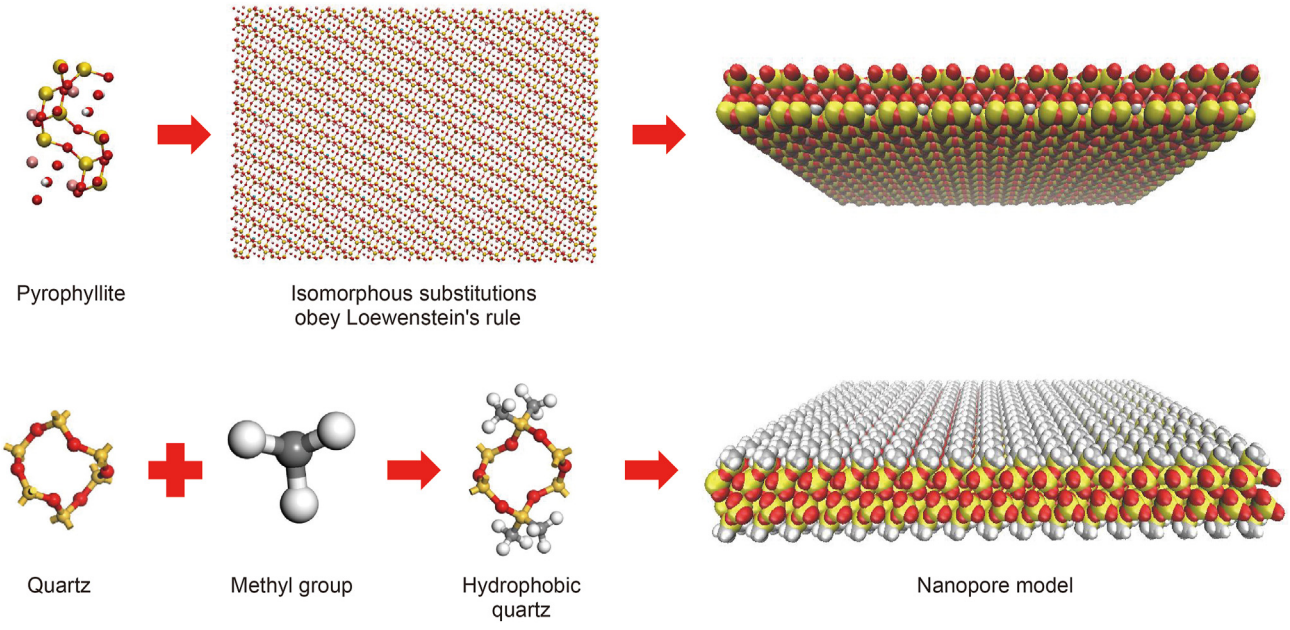

Fig. 1. Graphical demonstration of initializing the nanopore model. Atoms are displayed as silver (C), white (H), blue (N), yellow (Si), and red (O).

Table 1
Number of molecules for each simulation system.

System	$N_{saturates}$	$N_{aromatics}$	$N_{resin\ 1}$	$N_{resin\ 2}$	$N_{asphaltene}$	N_{SDBS}	N_{H_2O}	N_{Na^+}	N_{K^+}
QUA	9	8	9	9	3	8	7000	8	0
MON	9	8	9	9	3	8	7000	98	0
ILL	9	8	9	9	3	8	7000	8	120
Gibbsite	9	8	9	9	3	8	7000	8	0
Siloxane	9	8	9	9	3	8	7000	8	0

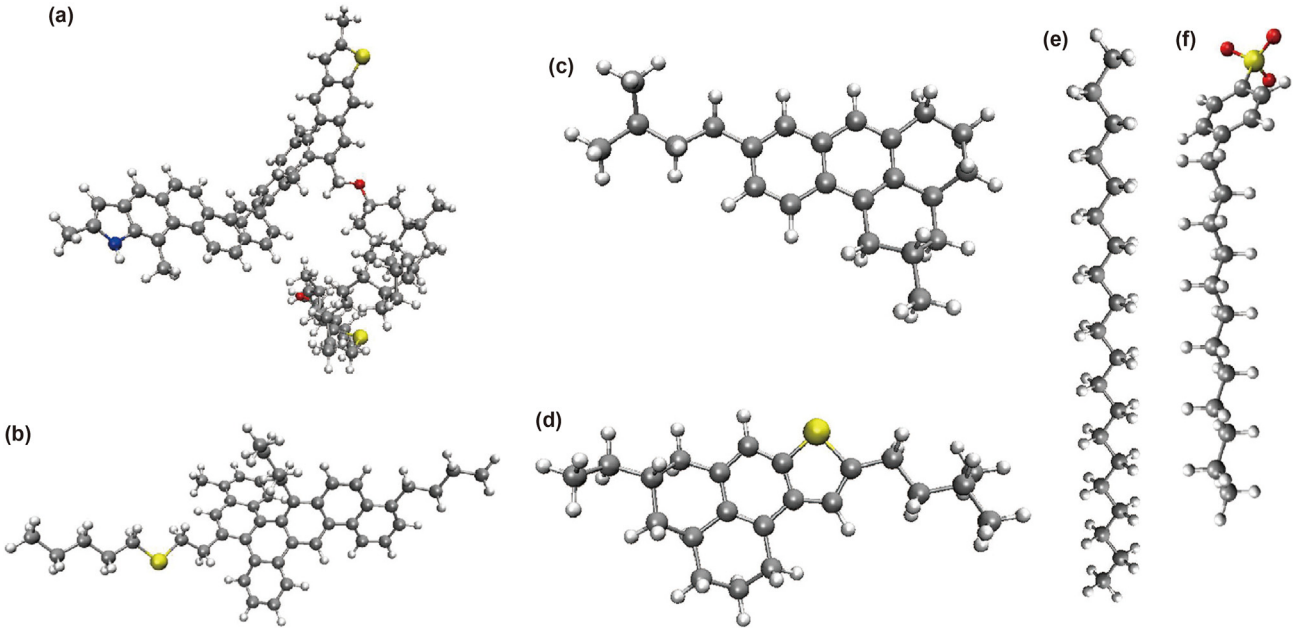

Fig. 2. Molecular structures of asphaltene ($C_{86}H_{99}NO_2S_2$) (**a**), aromatics ($C_{46}H_{50}S$) (**b**), resin 1 ($C_{23}H_{30}$) (**c**), resin 2 ($C_{22}H_{30}S$) (**d**), saturates ($C_{20}H_{42}$) (**e**), and SDBS ($C_{18}H_{29}O_3S$) (**f**). Atoms are displayed as silver (C), white (H), blue (N), yellow (S), and red (O).

Table 2
L–J parameters and atomic charge.

	Atomic species	Symbol	Mass, g/mol	Charge, e	E, kJ mol^{-1}	σ, Å
Clay/quartz	Aqueous sodium ion	Na	22.99	1	0.5443384	2.35
	Aqueous potassium ion	K	39.098	1	0.4184	3.334
	Hydroxyl hydrogen	ho	1.00797	0.425	0	0
	Hydroxyl oxygen	oh	15.9994	−0.95	0.6501936	3.1655
	Hydroxyl oxygen with substitution	ohs	15.9994	−1.808	0.6501936	3.1655
	Bridging oxygen	ob	15.9994	−1.05	0.6501936	3.1665
	Bridging oxygen with octahedral substitution	obos	15.9994	−1.1808	0.6501936	3.1665
	Bridging oxygen with tetrahedral substitution	obts	15.9994	−1.1688	0.6501936	3.1665
	Tetrahedral silicon	st	28.085	2.1	7.70065E-06	3.302
	Octahedral aluminum	ao	26.982	1.575	5.56388E-06	4.2712
	Tetrahedral aluminum	at	26.982	1.575	7.70065E-06	3.302
	Octahedral magnesium	MgO	24.305	1.36	3.77807E-06	5.2643
	Tetrahedral silicon with methyl group	sc	28.085	1.05	7.70406E-06	3.302
	Methyl carbon	cs	12.011	−0.18	0.276144	3.5
	Methyl hydrogen	hc	1.00797	0.06	0.12552	2.5
Water	Hydrogen	hw	1.00797	0.4238	0	0
SPC/E	Oxygen	ow	15.9994	−0.8476	0.6501936	3.166

software package (Abraham et al., 2015). The periodic boundary conditions were applied in three directions. The initial configurations for all the systems were constructed by the PACKMOL package (Martínez et al., 2009). The orthogonal simulation boxes were created with approximate lateral sizes $x = 64$ Å and $y = 92$ Å. Furthermore, a certain amount of Na^+ and K^+ were randomly placed in the nanopores to neutralize the electronegativity caused by montmorillonite, illite, and SDBS surfactant. The leap-frog algorithm was used to update the simulation models (Gunsteren and Berendsen, 1988). After initializing the simulation boxes, the energy minimization task was carried out to eliminate unphysical contacts between molecules. The steepest descent algorithm was implemented for energy minimization, and the upper limit of force between any pair of atoms was set to 1000 kJ/(mol nm). Then, the structure-optimized configuration was relaxed with a shorter timestep of 0.5 fs for 5 ns in an isothermal-isobaric (NPT) ensemble

under 5 MPa and 498 K, which is a typical reservoir condition for the steam-assisted gravity drainage (SAGD) process (Ahmadi and Chen, 2021b; Li et al., 2009; Nguyen et al., 2012). After the relaxation, the system was equilibrated in an NPT ensemble for 25 ns under 5 MPa and 498 K. The temperature of the equilibration stage was controlled by a velocity-rescale thermostat with a time constant of 0.5 ps, and the pressure of the equilibration stage was controlled by a Berendsen barostat (Berendsen et al., 1984; Bussi et al., 2007). Finally, an extra 50 ns simulation in an NPT ensemble was carried out for the production stage with a longer timestep of 1 fs. A Nosé-Hoover thermostat and a Parrinello–Rahman barostat were applied for temperature and pressure control in the production stage with the same time constant of 0.5 ps (Evans and Holian, 1985; Parrinello and Rahman, 1981). Pressure coupling was isotropic in the *x* and *y* directions; the *z* dimension was scaled independently. Meanwhile, the van der Waals (VDW) interactions were calculated by the atomic-based summation method with a cutoff distance of 1.2 nm. Long-range electrostatic interactions were evaluated by the particle-mesh Ewald (PME) method (Darden et al., 1993). All the atoms in the clay and quartz layers remain rigid to avoid distortion of the mineral layers and shorten the simulation time. Studies have reported that the impact of structure flexibility or rigidity on the distributions of water and hydrocarbon molecules is insignificant (He et al., 2017, 2021; Mi et al., 2022).

3. Results and discussion

Fig. 3 demonstrates snapshots of the configurations of the simulation systems for the bitumen detachment process from hydrophobic quartz surfaces after equilibration. These configurations are pivotal for understanding the dynamic interplay of molecules in these simulated environments. It should be noted that the QUA system is presented as a reference scenario, enabling comparative analysis with other systems and serving as a baseline for observations. Fig. 4 complements the insights from Fig. 3 by presenting the density distribution of each molecule type, including water, bitumen, SDBS, and ions in the *z* direction for all simulations. As mentioned, Fig. 4(a) illustrates the base case scenario for all systems for comparison purposes. As shown in Fig. 3, it is found that the negative-charged clay surface (MON and ILL systems) can adsorb the ions (Na^+ and K^+) and form a dense layer of ions near the clay surface. These phenomena can also be confirmed from Fig. 4(b) and (c) that the ions form a sharp density peak height near the clay surfaces, and the peak height of the illite surface is higher than the montmorillonite surface. Additionally, Fig. 3 illustrates the efficient attachment of SDBS molecules at the interface between bitumen droplets and hydrophobic quartz surfaces. The hydrophobic tails and benzene connectors of SDBS actively engage with both the bitumen droplets and the quartz surface. Notably, the hydrophilic head of SDBS is oriented towards the surrounding water molecules, forming stable interfacial layers. It is worth noting that several surfactant monomers interact with kaolinite surfaces (gibbsite and siloxane systems) instead of the bitumen droplets and hydrophobic surfaces, indicating the hindrance of SDBS mobilization. This localized interaction slows the effective dispersion of SDBS molecules at the bitumen–water interface, influencing the overall bitumen detachment process.

3.1. Number density profiles

Fig. 4 illustrates the number density distributions of bitumen, water, SDBS, and ions along the *z* direction (normal direction to the quartz surface) inside the nanopores. As a useful complement of Fig. 4, Fig. S1 in the Supporting Information compares the physical density of water in each system with experimental data. In the QUA system, the quartz surfaces exhibit strong hydrophobicity as they repel water molecules to the middle region of the pore. This phenomenon has also appeared in our previous study (Ahmadi and Chen, 2022). It is also observed that the density profiles of water molecules in all clay-hosted systems have similar trends due to the similar layered arrangement of water molecules near the external surface of these clay minerals. Specifically, water molecules tend to adsorb on the surface of montmorillonite, illite, and kaolinite, forming an interfacial water layer. For the MON and ILL systems, the density peak of water molecules lies closer to the clay surface than that of Na^+ in the MON system (Fig. 4(b)). However, the opposite phenomena are observed on K^+ of ILL (Fig. 4(c)). This can be attributed to the tendency of Na^+ to form an out-sphere complex (i.e., binding to a siloxane surface through water molecules), while K^+ tends to form an inner-sphere (i.e., directly adsorbing on the siloxane surface) (Li et al., 2020; Sposito et al., 1999). Our results showed that the high temperature and bitumen do not affect the tendency of Na^+ and K^+ to form cation adsorption complexes. For the Gibbsite and siloxane systems, the two kaolinite surfaces show different affinities for water molecules. The gibbsite surface can form a denser interfacial layer than that of the siloxane surface. Interestingly, it is found that there is a small density peak of water molecules near the quartz surfaces inside the siloxane system (Fig. 4(e)), which overlaps with the density peak of SDBS molecules. This observation suggests that surfactant molecules can potentially bind some water molecules, creating a nanostructure between SDBS and water molecules. Fig. S2 in the Supporting Information validates this speculation as a radial distribution function of SDBS-water exhibits a peak value around 0.2 nm, indicating the formation of a hydration shell around the polar head group of SDBS. Such phenomena have been observed in previous studies (Ahmadi et al., 2023; Parra et al., 2020).

The number density profiles of SDBS molecules in MON and ILL systems have two peaks: one lies in the exact location of the bitumen density peak, and the other lies where we have 50% of the bitumen peak density. The first peak shows that SDBS molecules are adsorbed at the interface between quartz and bitumen, facilitating the detachment of oil droplets. The second one means that the rest of the SDBS molecules gather in the interface between water and bitumen. In contrast, the number density profiles of SDBS molecules in the gibbsite and siloxane systems show different trends. SDBS molecules inside the gibbsite system prefer to exist in the middle region of the nanopore as their hydrophilic head part is absorbed at the gibbsite surface due to the strong hydroxylation. In this case, SDBS molecules cannot efficiently contribute to the oil detachment process from the hydrophobic quartz surface. SDBS molecules inside the siloxane system exhibit the highest peak value near the quartz surface, indicating the strongest affinity for SDBS. It means that we expect strong interactions between the SDBS, bitumen, and hydrophobic surface.

3.2. Radial distribution functions (RDFs)

RDF is defined as the spatial distribution probability function of certain particles with respect to the coordinates of a particle, which can be used to evaluate the interactions between particles. To elaborate, a higher peak value in RDF means stronger particle interactions. We calculated the RDF of bitumen fractions and SDBS for all simulation systems. The corresponding data are shown in Fig. 5 and Table 3. The highest peak value for each simulation system is observed in either resin pairs or asphaltene–resin, indicating the strongest interaction among these fractions. In other words, resin pairs and asphaltene–resin formed an intermolecular structure around 6 Å. Similar phenomena have been found in our previous

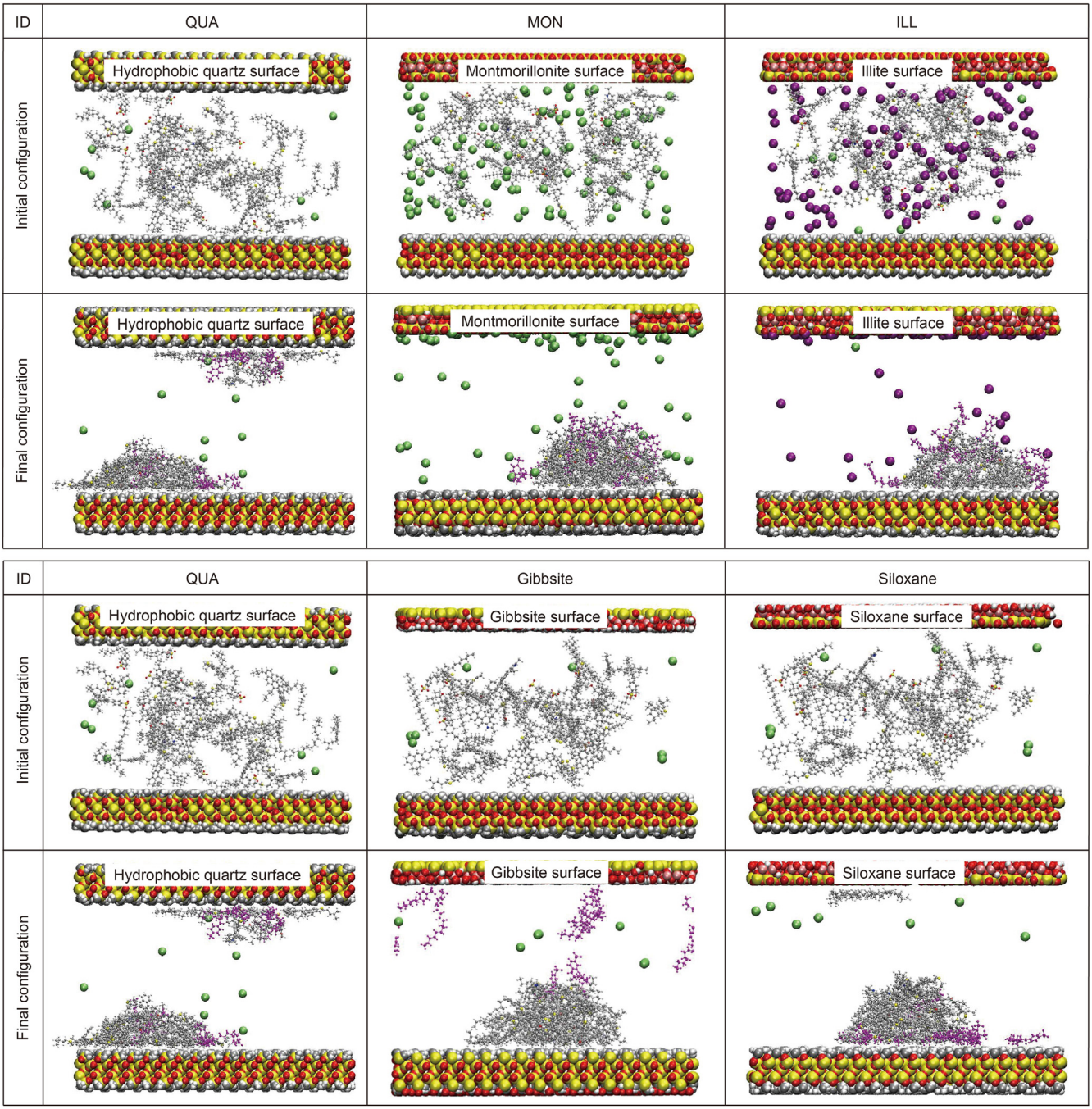

Fig. 3. Configuration of the simulation box for oil detachment process from the hydrophobic surface in clay-hosted nanopores Atoms are displayed as silver (C), white (H), blue (N), yellow (Si), red (O), lime (Na), and purple (K). Water molecules are hidden for the sake of transparency. SDBS molecules are dyed in magenta to observe their affinity at interfaces.

work, and we proved that the structure is caused by the non-covalent interactions of π–π stacking (Ahmadi and Chen, 2021a). Compared with other systems, the RDF curve of the SDBS pair in the Gibbsite system has a relatively flat trend, indicating a less concentrated spatial distribution. This finding is confirmed by configurations in Fig. 3 and number density profiles in Fig. 5. Moreover, according to our previous study, SDBS molecules tend to interact with asphaltene as they are the heaviest fraction of bitumen (Ahmadi and Chen, 2022). Combined this conclusion with the RDF results of the asphaltenes–SDBS in Fig. 5 and Tables 3 and it can be found that the strength of asphaltenes–SDBS interaction is weakened by the presence of montmorillonite and kaolinite surfaces. In contrast, the presence of an illite surface enhances this interaction. In this sense, during the steam–surfactant co-injection process, illite is conducive to bitumen production; montmorillonite and kaolinite are harmful.

3.3. Mean square displacement (MSD) and self-diffusivity (D)

In this study, we calculated the mean square displacement (MSD) and self-diffusivity of SDBS molecules to analyze their movement characteristics in the nanopores. MSD is often used to determine the deviation of a particle position to a reference position as a function of time. The slope of MSD with respect to time is

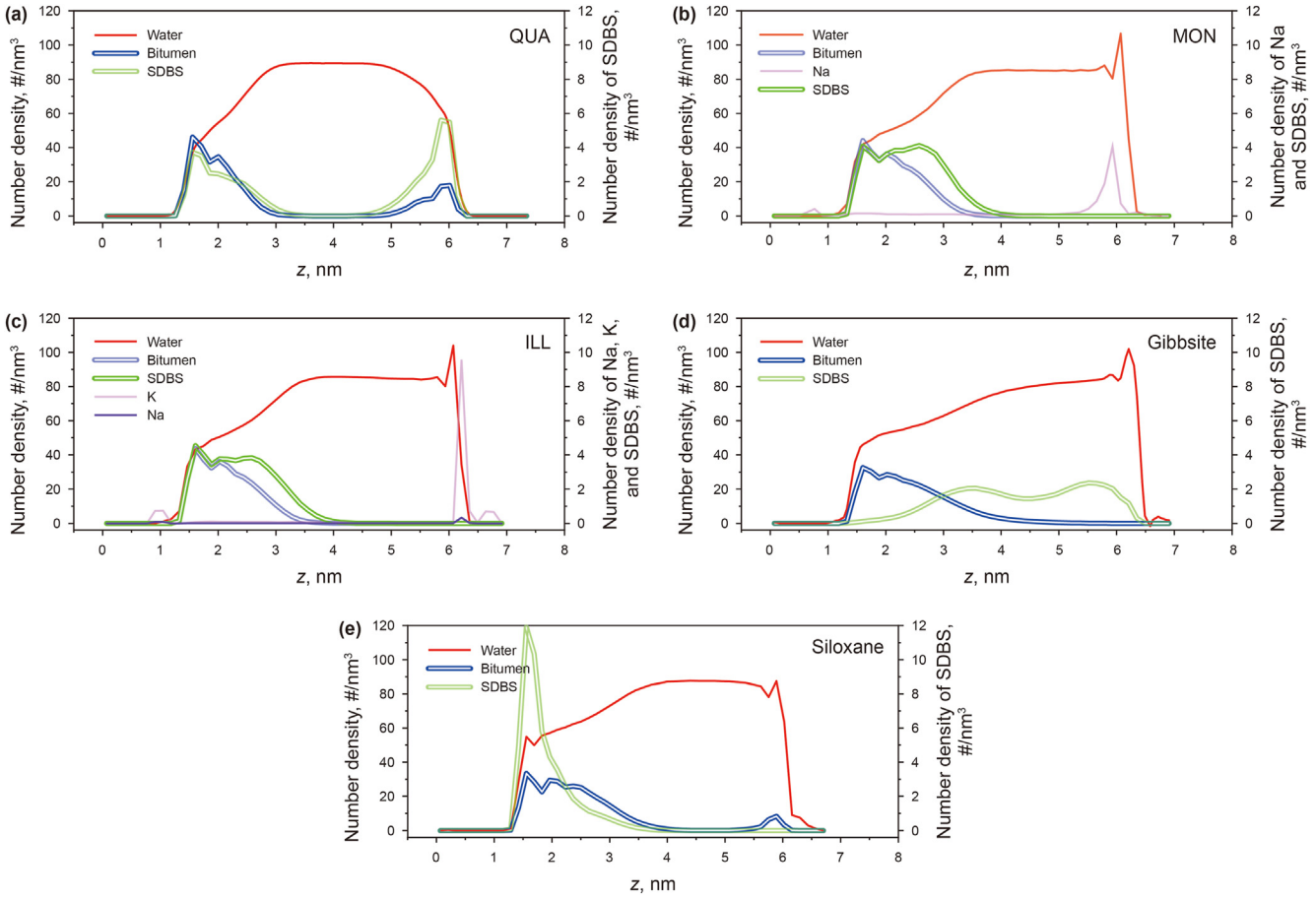

Fig. 4. Number density distribution of water, bitumen, SDBS, and ions in the *z* direction for all systems. (**a**) QUA; (**b**) MON; (**c**) ILL, (**d**) Gibbsite; (**e**) Siloxane. All profiles are averaged during the last 25 ns of simulation.

correlated to the self-diffusivity according to the Einstein relationship. To elaborate, MSD and self-diffusivity are calculated based on Eqs. (4) and (5), respectively:

$$\mathrm{MSD} = \frac{1}{N}\sum_{i=1}^{N}[r_i(t) - r_i(0)]^2 \tag{4}$$

$$D = \frac{1}{6N}\lim_{t\to\infty}\frac{\mathrm{d}}{\mathrm{d}t}\sum_{i=1}^{N}[r_i(t) - r_i(0)]^2 \tag{5}$$

where D is the self-diffusivity; N is the number of diffusing molecules; $r(t)$ and $r(0)$ are the position vectors of molecules at time t and $t = 0$, respectively.

Fig. 6 shows the MSD of SDBS molecules versus time for all simulation systems, and Fig. 7 illustrates the corresponding diffusivities. It is obvious that the clay mineral surfaces significantly influence the movement of SDBS surfactant inside the nanopores. In Fig. 7, the gibbsite system has the highest MSD, meaning that the SDBS molecules move freely and tend to exist in the water phase instead of the interface between quartz and bitumen. On the contrary, SDBS molecules in MON, siloxane, and ILL systems have significantly lower MSD than the QUA system. It can be speculated that montmorillonite, illite, and the siloxane surface of kaolinite restrain the movement of SDBS, thus enhancing the interaction of SDBS and bitumen and the hydrophobic quartz surface. This finding is confirmed by analyzing simulation configurations, number density profiles, and RDF curves.

3.4. Interaction energy analysis

To quantitatively investigate the interaction between bitumen and the hydrophobic surface, as well as the interaction between water and the hydrophobic quartz surface, the interaction energy analysis was carried out. Eqs. (6)–(8) defined the interaction energy between different molecules (Ahmadi and Chen, 2022; Zhong et al., 2013):

$$E_{\mathrm{bitumen-quartz}} = E_{\mathrm{bitumen+quartz}} - E_{\mathrm{bitumen}} - E_{\mathrm{quartz}} \tag{6}$$

$$E_{\mathrm{steam-quartz}} = E_{\mathrm{steam+quartz}} - E_{\mathrm{steam}} - E_{\mathrm{quartz}} \tag{7}$$

$$E_{\mathrm{steam-bitumen}} = E_{\mathrm{steam+bitumen}} - E_{\mathrm{bitumen}} - E_{\mathrm{steam}} \tag{8}$$

where $E_{\mathrm{bitumen+quartz}}$ is the total energy of bitumen molecules and the hydrophobic quartz surface; E_{bitumen} is the energy of the bitumen droplet; E_{quartz} is the energy of the hydrophobic quartz surface; E_{steam} is the steam phase energy; $E_{\mathrm{steam+quartz}}$ is the total energy of the steam phase and the hydrophobic quartz surface; $E_{\mathrm{steam+bitumen}}$ is the total energy of the steam phase and bitumen droplet.

Fig. 8 demonstrates the interaction energy between bitumen, steam, and the hydrophobic quartz surface pairs. A higher magnitude of the interaction energy between the quartz surface and

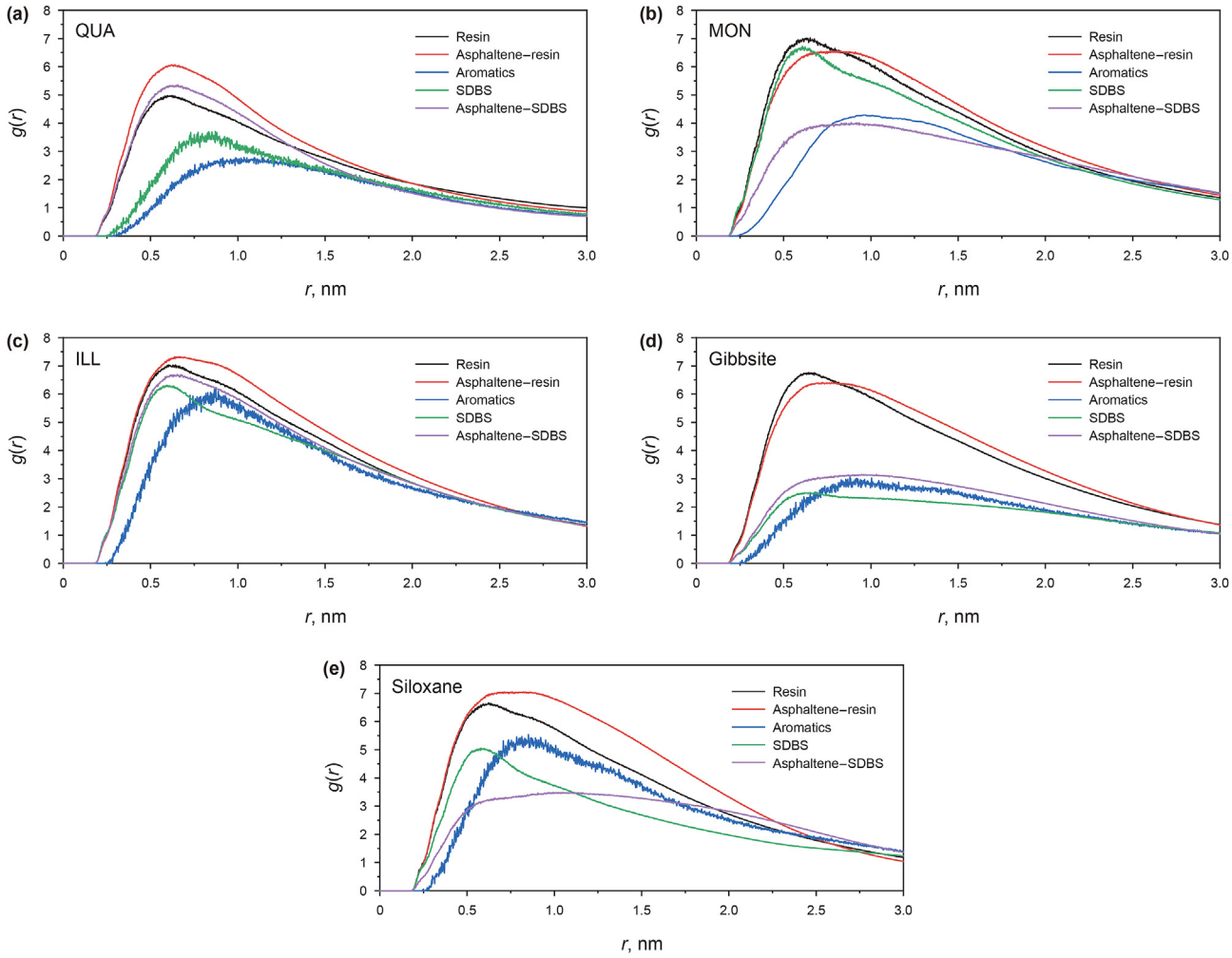

Fig. 5. Radial distribution function curves of molecule pairs for all simulation systems. (**a**) QUA; (**b**) MON; (**c**) ILL, (**d**) Gibbsite; (**e**) Siloxane. All curves are averaged during the last 25 ns of simulation.

Table 3
Peak values of specific pairs in radial distribution function curves.

System	QUA	MON	ILL	Gibbsite	Siloxane
Resin pair	4.987	7.026	7.037	6.767	7.051
Asphaltene–resin	6.072	6.592	7.324	6.406	6.668
Asphaltene–SDBS	5.355	4.018	6.704	3.152	3.485

bitumen means that the steam phase does not easily trip the bitumen droplets adhered to the quartz surface; hence, it is harder to separate the bitumen from the hydrophobic quartz surface. It is found in Fig. 8 that the interaction energy between steam and bitumen is greater than the interaction energy between bitumen and hydrophobic quartz. That means the ordered attachments of bitumen droplets on the hydrophobic quartz are very likely to be destroyed by steam, thereby facilitating the process of oil detachment. In addition, the higher the difference between these two interaction energies, the greater the likelihood that the oil detachment will occur. Therefore, according to Fig. 8, the probability of oil detachment from the hydrophobic quartz surface follows the order of siloxane > gibbsite > MON > ILL > QUA. Moreover, a conjecture can be made that the quartz lipophilicity is reduced when clay minerals are presented in nanopores, which deserves a thorough investigation in the future. The interaction energy analysis well reflects the effects of clay mineral surface on oil detachment.

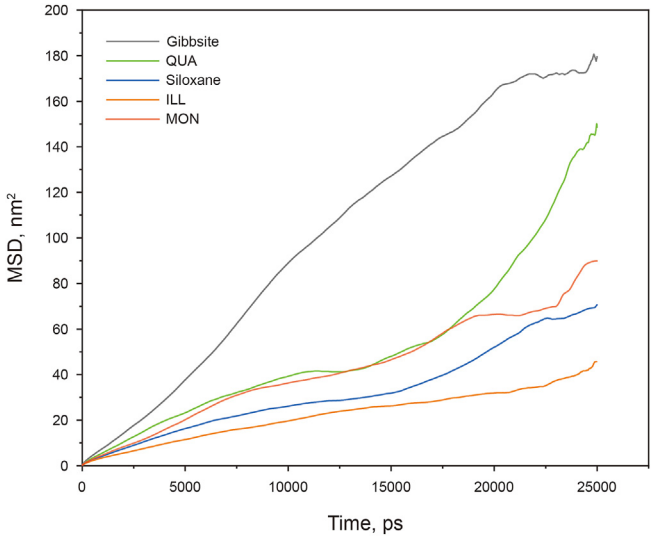

Fig. 6. MSD of SDBS molecules in all simulation systems.

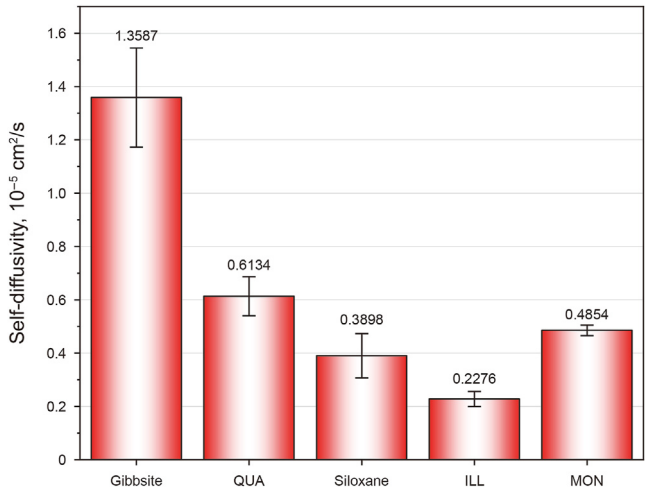

Fig. 7. Self-diffusivities of SDBS molecules in all simulation systems. Error bars represent the standard deviation calculated from block averages in GROMACS.

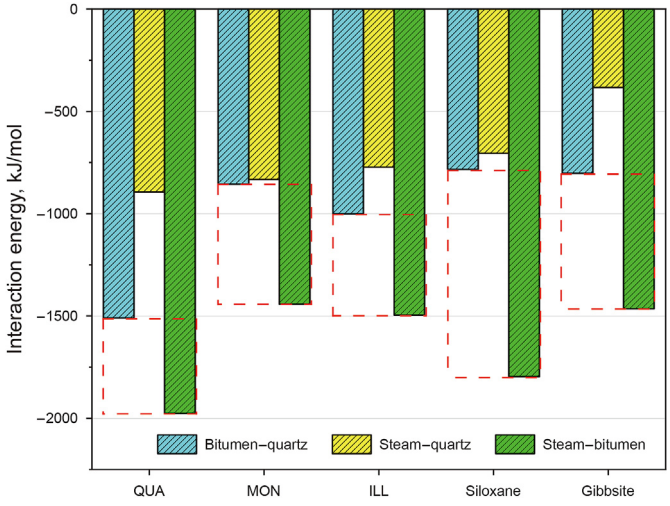

Fig. 8. Total interaction energy between bitumen droplets and quartz surface. Data are collected from the final configuration of molecular dynamics simulation.

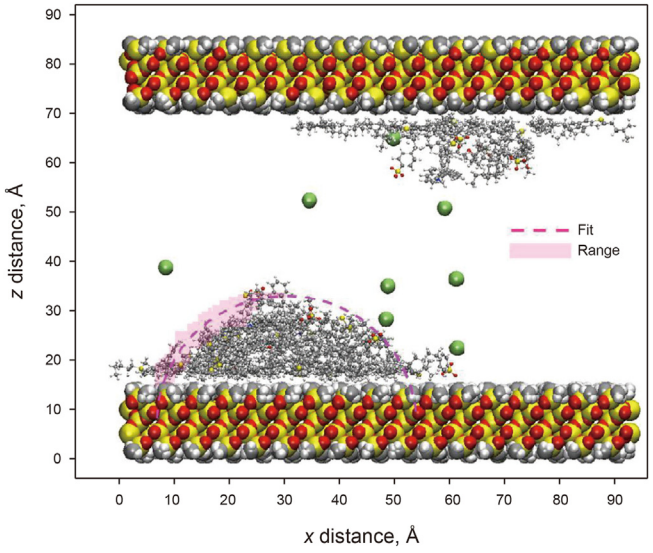

Fig. 9. Curvature of the bitumen–water interface in the x–z plane. The maximum and minimum of the coordinates are shown in the range of the pink area. The magenta dash line is the fit curve of the interface.

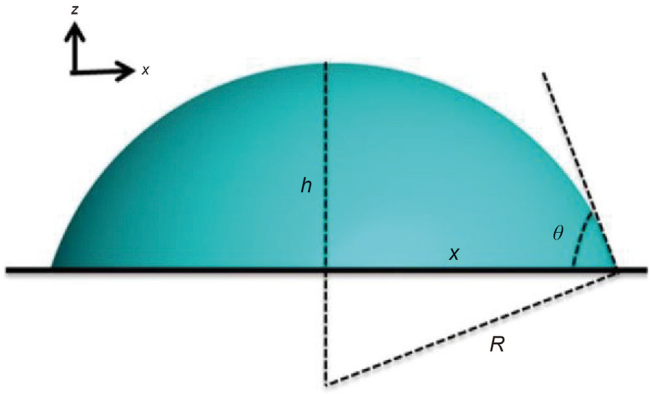

Fig. 10. Calculation of contact angles (Chang et al., 2018).

3.5. Contact angle–curvature of the bitumen–water–quartz interface

To measure the contact angle of bitumen on the hydrophobic quartz surface, we carried out a detailed analysis of the molecular trajectory data. A schematic illustration is shown in Fig. 9 for analyzing the QUA system. In short, the x, z coordinates of the interfacial molecules (regarded as the location where the water density is half of the bulk water density) were recorded every 1 ns of the simulation. The data shows significant fluctuance in the interfacial shape curve. Such fluctuations are regarded as the primary source of error in previous research works (Toledano et al., 2020; He and Nagel, 2019). Then, we adopted the optimal circular fit algorithm developed by Taubin to determine the curvature of the bitumen–water–quartz interface (Taubin, 1991). After obtaining all the radii from the Taubin method, the geometric method used by Chang et al. (2018) (Eqs. (9) and (10), Fig. 10) is implemented to calculate the contact angle:

$$x^2 + (R - h)^2 = R^2 \tag{9}$$

$$\cos\theta = \frac{R - h}{R} \tag{10}$$

where x is the half distance of the bitumen droplet spread on the substrate surface; h is the height from the center of the fitted circle to the substrate surface; R is the radius of the fitted circle; θ is the contact angle.

The corresponding results of the fitting radius and contact angles are listed in Table 4. It is worth mentioning that the contact angle in the QUA system is 54.9°, which is close to the projected value of 58.28° in the empirical equation at high temperature conditions in Duffy's experiments, verifying our simulation prediction of wetting behaviors (Duffy et al., 2021). Contact angles are often used as a measure of the rock wettability. Specifically, the hydrophobic quartz surface in the gibbsite has the largest contact angle, indicating it becomes more water-wet compared to other

Table 4
Contact angles of all simulation systems.

System	x, Å	R, Å	Contact angle, degree
QUA	22.870	27.593	54.9
MON	23.840	25.124	71.6
ILL	24.670	26.373	69.3
Gibbsite	21.440	22.238	74.6
Siloxane	20.085	21.558	68.7

systems. Such a change in the quartz wettability has been observed in previous experimental works and is regarded as a primary mechanism responsible for improved recoveries (Zaabi et al., 2023; Jonasson et al., 2018; Srivastava and Castro, 2011). Our results showed that the wettability of the hydrophobic quartz surface is strongly associated with the clay mineral surface presented in the nanopores. This finding also manifests that the contact angle measurements should take particular care to minimize or control the presence of clay contents as they complicate the rock mineralogy of the oil sands ore.

4. Conclusions

In this study, we used MD simulation methods to address the effect of clay minerals on the oil detachment from quartz surfaces during surfactant–steam co-injection. MD simulation was carried out to study the mechanisms of the oil detachment process of bitumen droplets under practical thermal recovery conditions in clay-hosted nanopores. Meanwhile, the number density profiles, radial distribution function curves, mean square displacements, interaction energies, and contact angles are explored. Based on the results, the following conclusions can be drawn:

(1) SDBS surfactant molecules tend to exist at the interfaces of bitumen–quartz and steam–quartz in QUA, MON, ILL, and siloxane systems. In contrast, SDBS surfactant molecules in the gibbsite system exist in the water phase. Only the hydrophilic head part of the SDBS molecules interacts with the strongly hydroxylated gibbsite surface.
(2) The gibbsite system has the highest MSD and the largest self-diffusivity, indicating that the presence of the gibbsite surface of kaolinite in nanopores causes the SDBS molecules to move freely instead of absorbing at the interface between bitumen droplets and the hydrophobic quartz surface. On the other hand, the presence of montmorillonite, illite, and the siloxane surface of kaolinite reduces the self-diffusivity of SDBS, improving the interactions between surfactant, quartz, and bitumen.
(3) The interaction energy analysis shows the probability of oil detachment from the hydrophobic quartz surface follows the order of siloxane > gibbsite > MON > ILL > QUA. The siloxane system has the largest interaction energy difference between the steam–bitumen and bitumen–quartz, indicating a straightforward oil detachment process.
(4) The presence of clay contents in the nanopores strongly influences the quartz wettability. All clay-hosted systems have larger contact angles than that of the QUA system. Specifically, the gibbsite system has the largest contact angle, exhibiting the strongest hydrophilicity.

CRediT authorship contribution statement

Ben-Jie-Ming Liu: Writing – original draft, Validation, Software, Methodology, Investigation, Formal analysis, Data curation, Conceptualization. **Xuan-Tong Lei:** Writing – original draft, Visualization, Software, Conceptualization. **Mohammadali Ahmadi:** Writing – review & editing, Methodology, Formal analysis. **Zhangxin Chen:** Writing – review & editing, Supervision, Methodology, Funding acquisition, Conceptualization.

Declaration of competing interest

The authors declare that they have no known competing financial interests or personal relationships that could have appeared to influence the work reported in this paper.

Acknowledgements

This research has been made possible by contributions from the Natural Sciences and Engineering Research Council (NSERC)/Energi Simulation Industrial Research Chair in Reservoir Simulation, the Alberta Innovates (iCore) Chair in Reservoir Modeling, the Energi Simulation/Frank and Sarsh Meyer Collaboration Centre.

Appendix A. Supplementary data

Supplementary data to this article can be found online at https://doi.org/10.1016/j.petsci.2024.04.004.

References

Abraham, M.J., Murtola, T., Schulz, R., Páll, S., Smith, J.C., Hess, B., Lindah, E., 2015. Gromacs: high performance molecular simulations through multi-level parallelism from laptops to supercomputers. SoftwareX 1–2, 19–25. https://doi.org/10.1016/j.softx.2015.06.001.
Ahmadi, M., Chen, Z., 2020. Challenges and future of chemical assisted heavy oil recovery processes. Adv. Colloid Interface Sci. 275, 102081. https://doi.org/10.1016/j.cis.2019.102081.
Ahmadi, M., Chen, Z., 2021a. Comprehensive molecular scale modeling of anionic surfactant-asphaltene interactions. Fuel 288, 119729. https://doi.org/10.1016/j.fuel.2020.119729.
Ahmadi, M., Chen, Z., 2021b. Spotlight onto surfactant–steam–bitumen interfacial behavior via molecular dynamics simulation. Sci. Rep. 11 (1). https://doi.org/10.1038/s41598-021-98633-1.
Ahmadi, M., Chen, Z., 2022. Molecular dynamics simulation of oil detachment from hydrophobic quartz surfaces during steam-surfactant co-injection. Energy 254. https://doi.org/10.1016/j.energy.2022.124434.
Ahmadi, M., Hou, Q., Wang, Y., Lei, X., Liu, B., Chen, Z., 2023. Spotlight on reversible emulsification and demulsification of tetradecane-water mixtures using CO_2/N_2 switchable surfactants: molecular dynamics (MD) simulation. Energy 279, 128100. https://doi.org/10.1016/j.energy.2023.128100.
Alshaikh, M., 2019. Anionic Surfactant and heavy oil interaction during surfactant-steam process. In: SPE Western Regional Meeting. https://doi.org/10.2118/195254-MS.
Andrés, E., Dominguez, H., Pizio, O., 2015. Temperature dependence of the microscopic structure and density anomaly of the SPC/E and TIP4P-Ew water models. Molecular dynamics simulation results. Condens. Matter Phys. 18 (1). https://doi.org/10.5488/CMP.18.13603.
Badu, S., Pimienta, I.S.O., Orendt, A.M., Pugmire, R.J., Facelli, J.C., 2012. Modeling of asphaltenes: assessment of sensitivity of ^{13}C solid state NMR to molecular structure. Energy Fuels. 26 (4), 2161–2167. https://doi.org/10.1021/ef201957q.
Bai, S., Kubelka, J., Piri, M., 2020. A positively charged calcite surface model for molecular dynamics studies of wettability alteration. J. Colloid Interface Sci. 569, 128–139. https://doi.org/10.1016/j.jcis.2020.02.037.
Banerjee, D., 2012. Oil Sands, Heavy Oil, & Bitumen from Recovery to Refinery, 2012th ed. PennWell Books, Tulsa, OK.
Batmunkh, M., Shearer, C.J., Biggs, M.J., Shapter, J.G., 2016. Solution processed graphene structures for perovskite solar cells. J. Mater. Chem. A 4 (7), 2605–2616. https://doi.org/10.1039/c5ta08996d.
Berendsen, H.J.C., Postma, J.P.M., van Gunsteren, W.F., DiNola, A., Haak, J.R., 1984. Molecular dynamics with coupling to an external bath. J. Chem. Phys. 81 (8), 3684–3690. https://doi.org/10.1063/1.448118.
Berendsen, H.J.C., Grigera, J.R., Straatsma, T.P., 1987. The missing term in effective pair potentials. J. Phys. Chem. 91, 6269–6271. https://doi.org/10.1021/j100308a038.
Bickmore, B.R., Rosso, K.M., Nagy, K.L., Cygan, R.T., Tadanier, C.J., 2003. *Ab initio* determination of edge surface structures for dioctahedral 2:1 phyli-osilicates: implications for acid-base reactivity. Clay Clay Miner. 51 (4), 359–371. https://doi.org/10.1346/CCMN.2003.0510401.
Bish, D.L., Von Dreele, R.B., 1989. Rietveld refinement of non-hydrogen atomic positions in kaolinite. Clay Clay Miner. 37 (4), 289–296. https://doi.org/10.1346/CCMN.1989.0370401.
Brockway, P.E., Owen, A., Brand-Correa, L.I., Hardt, L., 2019. Estimation of global final-stage energy-return-on-investment for fossil fuels with comparison to renewable energy sources. Nat. Energy 4 (7), 612–621. https://doi.org/10.1038/s41560-019-0425-z.
Bussi, G., Donadio, D., Parrinello, M., 2007. Canonical sampling through velocity rescaling. J. Chem. Phys. 126 (1), 014101. https://doi.org/10.1063/1.2408420.
Cao, Z., Jiang, H., Zeng, J., Saibi, H., Lu, T., Xie, X., Zhang, Y., Zhou, G., Wu, K., Guo, J., 2021. Nanoscale liquid hydrocarbon adsorption on clay minerals: a molecular dynamics simulation of shale oils. Chem. Eng. J. 420. https://doi.org/10.1016/j.cej.2020.127578.
Carrigy, M.A., 1966. Lithology of the Athabasca oil sands. RCA/AGS Bull. 18.
Chang, X., Xue, Q., Li, X., Zhang, J., Zhu, L., He, D., Zheng, H., Lu, S., Liu, Z., 2018.

Inherent wettability of different rock surfaces at nanoscale: a theoretical study. Appl. Surf. Sci. 434, 73–81. https://doi.org/10.1016/j.apsusc.2017.10.173.
Chen, M., Wang, Y., Chen, W., Ding, M., Zhang, Z., Zhang, C., Cui, S., 2023. Synthesis and evaluation of multi-aromatic ring copolymer as viscosity reducer for enhancing heavy oil recovery. Chem. Eng. J. 470, 144220. https://doi.org/10.1016/j.cej.2023.144220.
Cygan, R.T., Liang, J.J., Kalinichev, A.G., 2004. Molecular models of hydroxide, oxyhydroxide, and clay phases and the development of a general force field. J. Phys. Chem. B 108 (4), 1255–1266. https://doi.org/10.1021/jp0363287.
Cygan, R.T., Greathouse, J.A., Kalinichev, A.G., 2021. Advances in Clayff molecular simulation of layered and nanoporous materials and their aqueous interfaces. J. Phys. Chem. C 125 (32), 17573–17589. https://doi.org/10.1021/acs.jpcc.1c04600.
Czarnecki, J., Radoev, B., Schramm, L.L., Slavchev, R., 2005. On the nature of athabasca oil sands. Adv. Colloid Interface Sci. 114-115, 53–60. https://doi.org/10.1016/j.cis.2004.09.009.
Darden, T., York, D., Pedersen, L., 1993. Particle mesh Ewald: an $N\cdot\log(N)$ method for Ewald sums in large systems. J. Chem. Phys. 98 (12), 10089–10092. https://doi.org/10.1063/1.464397.
Davenport, J., Wayth, N., 2023. Statistical Review of World Energy 2023. British Petroleum, London.
Deng, Y., Wu, Q., Li, Z., Huang, X., Rao, S., Liang, Y., Lu, H., 2022. Crystal face dependent wettability of α-quartz: elucidation by time-of-flight secondary ion mass spectrometry techniques combined with molecular dynamics. J. Colloid Interface Sci. 607, 1699–1708. https://doi.org/10.1016/j.jcis.2021.09.047.
Deng, Y., Li, Z., Rao, S., Zheng, H., Huang, X., Liu, Q., Wang, D., Lu, H., 2023. Mechanism for the effects of surface chemical composition and crystal face on the wettability of α-quartz surface. Appl. Surf. Sci. 633. https://doi.org/10.1016/j.apsusc.2023.157559.
Ding, B., Nie, Z., Li, Z., Dong, M., 2021. Emulsion-assisted thermal recovery method in heterogeneous oilsands reservoir. J. Petrol. Sci. Eng. 197. https://doi.org/10.1016/j.petrol.2020.108113.
Ding, F., Gao, M., 2021. Pore wettability for enhanced oil recovery, contaminant adsorption and oil/water separation: a review. Adv. Colloid Interface Sci. 289. https://doi.org/10.1016/j.cis.2021.102377.
Dodda, L.S., Cabeza de Vaca, I., Tirado-Rives, J., Jorgensen, W.L., 2017. LigParGen web server: an automatic OPLS-AA parameter generator for organic ligands. Nucleic Acids Res. 45 (W1), W331–W336. https://doi.org/10.1093/nar/gkx312.
Drits, V.A., Zviagina, B.B., McCarty, D.K., Salyn, A.L., 2010. Factors responsible for crystal-chemical variations in the solid solutions from illite to aluminoceladonite and from glauconite to celadonite. Am. Mineral. 95 (2–3), 348–361. https://doi.org/10.2138/am.2010.3300.
Duffy, T.S., Li, J., Johns, R.T., Lvov, S.N., 2021. Capillary contact angle for the quartz-distilled water-normal decane interface at temperatures up to 200 °C. Colloids Surf. A Physicochem. Eng. Asp. 609, 125608. https://doi.org/10.1016/j.colsurfa.2020.125608.
Dusseault, M.B., Scafe, D., 1979. Mineralogical and engineering index properties of the basal McMurray Formation clay shales. Can. Geotech. J. 16, 285–294.
Entezari, I., Rivard, B., Geramian, M., Lipsett, M.G., 2017. Predicting the abundance of clays and quartz in oil sands using hyperspectral measurements. Int. J. Appl. Earth Obs. Geoinf. 59, 1–8. https://doi.org/10.1016/j.jag.2017.02.018.
Evans, D.J., Holian, B.L., 1985. The nose-hoover thermostat. J. Chem. Phys. 83 (8), 4069–4074. https://doi.org/10.1063/1.449071.
Ghaleh, P.S., Khodapanah, E., Tabatabaei-Nezhad, S.A., 2020. Comprehensive monolayer two-parameter isotherm and kinetic studies of thiamine adsorption on clay minerals: experimental and modeling approaches. J. Mol. Liq. 306. https://doi.org/10.1016/j.molliq.2020.112942.
Gunsteren, W.F., Berendsen, H.J.C., 1988. A leap-frog algorithm for stochastic dynamics. Mol. Simulat. 1 (3), 173–185. https://doi.org/10.1080/08927028808080941.
Han, X., Feng, F., Zhang, J., 2023. Study on the whole life cycle integrity of cement interface in heavy oil thermal recovery well under circulating high temperature condition. Energy 278. https://doi.org/10.1016/j.energy.2023.127873.
He, M., Nagel, S.R., 2019. Characteristic interfacial structure behind a rapidly moving contact line. Phys. Rev. Lett. 122 (1), 18001. https://doi.org/10.1103/PhysRevLett.122.018001.
He, Z., Linga, P., Jiang, J., 2017. CH_4 hydrate formation between silica and graphite surfaces: insights from microsecond molecular dynamics simulations. Langmuir 33 (43), 11956–11967. https://doi.org/10.1021/acs.langmuir.7b02711.
He, Z., Mi, F., Ning, F., 2021. Molecular insights into CO_2 hydrate formation in the presence of hydrophilic and hydrophobic solid surfaces. Energy 234, 121260. https://doi.org/10.1016/j.energy.2021.121260.
Hooshiar, A., Uhlik, P., Ivey, D.G., Liu, Q., Etsell, T.H., 2012. Clay minerals in nonaqueous extraction of bitumen from Alberta oil sands: Part 2. Characterization of clay minerals. Fuel Process. Technol. 96, 183–194. https://doi.org/10.1016/j.fuproc.2011.10.010.
Jia, H., Lian, P., Yan, H., Yuan, J., Tang, H., Wei, X., Song, J., He, J., Lv, K., Liu, D., 2021. Novel molecular insight into the discrepant distributions for ionic surfactants in light oil/water and heavy oil/water systems. Fuel 304. https://doi.org/10.1016/j.fuel.2021.121460.
Jonasson, R.G., Imran, M., Knorr, K.D., 2018. Screening surfactants for application in SAGD-including a steam-phase coreflood test. In: SPE Canada Heavy Oil Technical Conference. https://doi.org/10.2118/189760-MS.
Jorgensen, W.L., Maxwell, D.S., Tirado-Rives, J., 1996. Development and testing of the OPLS all-atom force field on conformational energetics and properties of organic liquids. J. Am. Chem. Soc. 118 (45), 11225–11236. https://doi.org/10.1021/ja9621760.
Kaminsky, H.A.W., Etsell, T.H., Ivey, D.G., Omotoso, O., 2009. Distribution of clay minerals in the process streams produced by the extraction of bitumen from athabasca oil sands. Can. J. Chem. Eng. 87 (1), 85–93. https://doi.org/10.1002/cjce.20133.
Koleini, M.M., Badizad, M.H., Ayatollahi, S., 2019. An atomistic insight into interfacial properties of brine nanofilm confined between calcite substrate and hydrocarbon layer. Appl. Surf. Sci. 490, 89–101. https://doi.org/10.1016/j.apsusc.2019.05.337.
Kong, L., Yang, M., Wang, H., Peng, Y., Zhu, S., Shao, Q., 2023. Study on the effect of sulfonic acid root position on the stability of SDBS emulsified asphalt. Construct. Build. Mater. 396. https://doi.org/10.1016/j.conbuildmat.2023.132303.
Li, A., Li, R., Yan, C., Wang, H., Liu, Q., Masliyah, J.H., Zeng, H., Xu, Z., 2023. The effect of clay type and solid wettability on bitumen extraction from Canadian oil sands. Fuel 337. https://doi.org/10.1016/j.fuel.2022.126887.
Li, P., Chan, M., Froehlich, W., 2009. Steam injection pressure and the SAGD ramp-up process. J. Can. Petrol. Technol. 48 (1), 36–41. https://doi.org/10.2118/09-01-36.
Li, Xiaofang, Wang, P., Yan, Z., Yu, S., Wei, K., Zhu, X., Sun, Y., Xue, Q., 2022. The miscible behaviors of C_3H_8/C_8H_{18}($C_7H_{17}N$) system in nanoslits: effects of pore size and rock surface wettability. Chem. Eng. J. 431. https://doi.org/10.1016/j.cej.2021.133988.
Li, X., He, L., Wu, G., Sun, W., Li, H., Sui, H., 2012. Operational parameters, evaluation methods, and fundamental mechanisms: aspects of nonaqueous extraction of bitumen from oil sands. Energy Fuels. 26 (6), 3553–3563. https://doi.org/10.1021/ef300337q.
Li, Y., Chen, M., Song, H., Yuan, P., Zhang, B., Liu, D., Zhou, H., Bu, H., 2020. Effect of cations (Na^+, K^+, and Ca^{2+}) on methane hydrate formation on the external surface of montmorillonite: insights from molecular dynamics simulation. ACS Earth Space Chem. 4 (4), 572–582. https://doi.org/10.1021/acsearthspacechem.9b00323.
Liu, J., Xu, Z., Masliyah, J., 2004. Role of fine clays in bitumen extraction from oil sands. AIChE J. 50 (8), 1917–1927. https://doi.org/10.1002/aic.10174.
Liu, Z., Wang, H., Blackbourn, G., Feng, M.A., Zhengjun, H.E., Wen, Z., Wang, Z., Yang, Z., Luan, T., Zhenzhen, W.U., 2019. Heavy oils and oil sands: global distribution and resource assessment. Acta Geol. Sin. 93 (1), 199–212. https://doi.org/10.1111/1755-6724.13778.
Loewenstein, M., 1954. The distribution of aluminum in the tetrahedra of silicates and aluminates. Am. Mineral. 39, 92–96.
Lu, Y., Li, R., Manica, R., Zhang, Z., Liu, Q., Xu, Z., 2022. CO_2-responsive surfactants for greener extraction of heavy oil: a bench-scale demonstration. J. Clean. Prod. 338. https://doi.org/10.1016/j.jclepro.2022.130554.
Lv, Q., Li, Z., Li, B., Li, S., Sun, Q., 2015. Study of nanoparticle-surfactant-stabilized foam as a fracturing fluid. Ind. Eng. Chem. Res. 54 (38), 9456–9477. https://doi.org/10.1021/acs.iecr.5b02197.
Martínez, L., Andrade, R., Birgin, E.G., Martínez, J.M., 2009. PACKMOL: a package for building initial configurations for molecular dynamics simulations. J. Comput. Chem. 30 (13), 2157–2164. https://doi.org/10.1002/jcc.21224.
Mi, F., He, Z., Zhao, Y., Jiang, G., Ning, F., 2022. Effects of surface property of mixed clays on methane hydrate formation in nanopores: a molecular dynamics study. J. Colloid Interface Sci. 627, 681–691. https://doi.org/10.1016/j.jcis.2022.07.101.
Nguyen, H.X., Wisup, B., Tran, X.V., Ta, D.Q., Nguyen, D.H., 2012. Effects of reservoir parameters and operational design on the prediction of SAGD performance in Athabasca Oilsands. In: SPE Europec/EAGE Annual Conference. https://doi.org/10.2118/154778-MS.
Parra, J.G., Iza, P., Dominguez, H., Schott, E., Zarate, X., 2020. Effect of Triton X-100 surfactant on the interfacial activity of ionic surfactants SDS, CTAB and SDBS at the air/water interface: a study using molecular dynamic simulations. Colloids Surf. A Physicochem. Eng. Asp. 603, 125284. https://doi.org/10.1016/j.colsurfa.2020.125284.
Parrinello, M., Rahman, A., 1981. Polymorphic transitions in single crystals: a new molecular dynamics method. J. Appl. Phys. 52 (12), 7182–7190. https://doi.org/10.1063/1.328693.
Refson, K., Park, S.H., Sposito, G., 2003. *Ab initio* computational crystallography of 2: 1 clay minerals: 1. Pyrophyllite-1Tc. J. Phys. Chem. B 107 (48), 13376–13383. https://doi.org/10.1021/jp0347670.
Rui, Z., Wang, X., Zhang, Z., Lu, J., Chen, G., Zhou, X., Patil, S., 2018. A realistic and integrated model for evaluating oil sands development with Steam Assisted Gravity Drainage technology in Canada. Appl. Energy 213, 76–91. https://doi.org/10.1016/j.apenergy.2018.01.015.
Sposito, G., Skipper, N.T., Sutton, R., Park, S.-H., Soper, A.K., Greathouse, J.A., 1999. Surface geochemistry of the clay minerals. Proc. Natl. Acad. Sci. USA 96, 3358–3364. https://doi.org/10.1073/pnas.96.7.3358.
Srivastava, P., Castro, L., 2011. Successful field application of surfactant additives to enhance thermal recovery of heavy oil. In: SPE/CIM International Conference on Horizontal Well Technology. https://doi.org/10.2118/65482-MS.
Su, G., Zhang, H., Geng, T., Yuan, S., 2019. Effect of SDS on reducing the viscosity of heavy oil: a molecular dynamics study. Energy Fuels. 33 (6), 4921–4930. https://doi.org/10.1021/acs.energyfuels.9b00006.
Tackie-Otoo, B.N., Ayoub Mohammed, M.A., Yekeen, N., Negash, B.M., 2020. Alternative chemical agents for alkalis, surfactants and polymers for enhanced oil recovery: research trend and prospects. J. Petrol. Sci. Eng. 187. https://doi.org/10.1016/j.petrol.2019.106828.
Tajik, A., Farhadian, A., Khelkhal, M.A., Rezaeisadat, M., Petrov, S.M., Eskin, A.A., Vakhin, A.V., Babapour Golafshani, M., Lapuk, S.E., Buzurov, A.E., Kiiamov, A.,

Ancheyta, J., 2023. Sunflower oil as renewable biomass source to develop highly effective oil-soluble catalysts for in-situ combustion of heavy oil. Chem. Eng. J. 453. https://doi.org/10.1016/j.cej.2022.139813.
Tang, W., Wu, P., Da, C., Alzobaidi, S., Harris, J., Hallaman, B., Hu, D., Johnston, K.P., 2023. Synergy of surface modified nanoparticles and surfactant in wettability alteration of calcite at high salinity and temperature. Fuel 331. https://doi.org/10.1016/j.fuel.2022.125752.
Taubin, G., 1991. Estimation of planar curves, surfaces,and nonplanar space curves defined by implicit equations with applications to edge and range image segmentation. IEEE Trans. Pattern Anal. Mach. Intell. 13 (11), 1115–1138. https://doi.org/10.1109/34.103273.
Tetteh, J., Bai, S., Kubelka, J., Piri, M., 2022. Wettability reversal on oil-wet calcite surfaces: experimental and computational investigations of the effect of the hydrophobic chain length of cationic surfactants. J. Colloid Interface Sci. 619, 168–178. https://doi.org/10.1016/j.jcis.2022.03.114.
Tian, H., Liu, F., Jin, X., Wang, M., 2019a. Competitive effects of interfacial interactions on ion-tuned wettability by atomic simulations. J. Colloid Interface Sci. 540, 495–500. https://doi.org/10.1016/j.jcis.2018.12.108.
Tian, S., Erastova, V., Lu, S., Greenwell, H.C., Underwood, T.R., Xue, H., Zeng, F., Chen, G., Wu, C., Zhao, R., 2018. Understanding model crude oil component interactions on kaolinite silicate and aluminol surfaces: toward improved understanding of shale oil recovery. Energy Fuels. 32 (2), 1155–1165. https://doi.org/10.1021/acs.energyfuels.7b02763.
Tian, S., Wang, T., Li, G., Sheng, M., Zhang, P., 2019b. Nanoscale surface properties of organic matter and clay minerals in shale. Langmuir 35 (17), 5711–5718. https://doi.org/10.1021/acs.langmuir.9b00157.
Toledano, J.-C., Blake, T.D., De Coninck, J., 2020. Moving contact lines and Langevin formalism. J. Colloid Interface Sci. 562, 287–292. https://doi.org/10.1016/j.jcis.2019.11.123.
Tosuai, T., Thanasaksukthawee, V., Lu, Y., Akamine, T., Somprasong, K., Tangparitkul, S., 2023. Enhanced bitumen extraction from oil sands using CO_2-responsive surfactant combined with low-salinity brine: toward cleaner production via CO_2 utilization. Colloids Surf. A Physicochem. Eng. Asp. 670. https://doi.org/10.1016/j.colsurfa.2023.131617.
Underwood, T., Erastova, V., Cubillas, P., Greenwell, H.C., 2015. Molecular dynamic simulations of montmorillonite organic interactions under varying salinity: an insight into enhanced oil recovery. J. Phys. Chem. C 119 (13), 7282–7294. https://doi.org/10.1021/acs.jpcc.5b00555.
Verstraete, J.J., Schnongs, P., Dulot, H., Hudebine, D., 2010. Molecular reconstruction of heavy petroleum residue fractions. Chem. Eng. Sci. 65 (1), 304–312. https://doi.org/10.1016/j.ces.2009.08.033.
Wang, D., Li, C., Seright, R.S., 2020. Laboratory evaluation of polymer retention in a heavy oil sand for a polymer flooding application on Alaska's north slope. SPE J. 25 (4), 1842–1856. https://doi.org/10.2118/200428-PA.
Wang, R., Liao, B., Wang, J., Sun, J., Wang, Y., Wang, J., Wang, Q., Qu, Y., Cheng, R., 2023. Microscopic molecular insights into methane hydrate growth on the surfaces of clay minerals: experiments and molecular dynamics simulations. Chem. Eng. J. 451. https://doi.org/10.1016/j.cej.2022.138757.
Wang, Z., Wang, Q., Jia, C., Bai, J., 2022. Thermal evolution of chemical structure and mechanism of oil sands bitumen. Energy 244. https://doi.org/10.1016/j.energy.2022.123190.
Welsby, D., Price, J., Pye, S., Ekins, P., 2021. Unextractable fossil fuels in a 1.5 °C world. Nature 597 (7875), 230–234. https://doi.org/10.1038/s41586-021-03821-8.
Wu, G., Zhu, X., Ji, H., Chen, D., 2015. Molecular modeling of interactions between heavy crude oil and the soil organic matter coated quartz surface. Chemosphere 119, 242–249. https://doi.org/10.1016/j.chemosphere.2014.06.030.
Xie, Y., Khishvand, M., Piri, M., 2020. Wettability of calcite surfaces: impacts of brine ionic composition and oil phase polarity at elevated temperature and pressure conditions. Langmuir 36 (22), 6079–6088. https://doi.org/10.1021/acs.langmuir.0c00367.
Xiong, H., Devegowda, D., 2022. Fluid behavior in clay-hosted nanopores with varying salinity: insights into molecular dynamics. SPE J. 27 (3), 1396–1410. https://doi.org/10.2118/209212-PA.
Yang, Y., Liang, X., Li, X., 2023. Investigation of clay-oil interfacial interactions in petroleum-contaminated soil: effect of crude oil composition. J. Mol. Liq. 380. https://doi.org/10.1016/j.molliq.2023.121702.
Zaabi, A., Arif, M., Ali, M., Adila, A., Abbas, Y., Kumar, R.S., Keshavarz, A., Iglauer, S., 2023. Impact of carbonate mineral heterogeneity on wettability alteration potential of surfactants. Fuel 342, 127819. https://doi.org/10.1016/j.fuel.2023.127819.
Zhan, S., Su, Y., Jin, Z., Wang, W., Cai, M., Li, L., Hao, Y., 2020. Molecular insight into the boundary conditions of water flow in clay nanopores. J. Mol. Liq. 311, 113292. https://doi.org/10.1016/j.molliq.2020.113292.
Zhang, H., Cao, J., Duan, H., Luo, H., Liu, X., 2022. Molecular dynamics insight into the adsorption and distribution of bitumen subfractions on Na-montmorillonite surface. Fuel 310. https://doi.org/10.1016/j.fuel.2021.122380.
Zhang, L., Lu, X., Liu, X., Yang, K., Zhou, H., 2016. Surface wettability of basal surfaces of clay minerals: insights from molecular dynamics simulation. Energy Fuels. 30 (1), 149–160. https://doi.org/10.1021/acs.energyfuels.5b02142.
Zhang, M., Nan, Y., Lu, Y., You, Q., Jin, Z., 2023. CO_2-responsive surfactant for oil-in-water emulsification and demulsification from molecular perspectives. Fuel 331. https://doi.org/10.1016/j.fuel.2022.125773.
Zhong, J., Wang, P., Zhang, Y., Yan, Y., Hu, S., Zhang, J., 2013. Adsorption mechanism of oil components on water-wet mineral surface: a molecular dynamics simulation study. Energy 59, 295–300. https://doi.org/10.1016/j.energy.2013.07.016.